

Published in final edited form as:

Nat Neurosci. 2015 September ; 18(9): 1291–1298. doi:10.1038/nn.4072.

Hippocampal circuit dysfunction in the Tc1 mouse model of Down syndrome

J. Witton^{#1}, R. Padmashri^{#2,10}, L.E. Zinyuk^{#1}, V.I. Popov^{4,5,*}, I. Kraev⁵, S.J. Line⁷, T.P. Jensen², A. Tedoldi⁸, D.M. Cummings⁸, V.L.J. Tybulewicz⁶, E.M.C. Fisher³, D.M. Bannerman⁷, A.D. Randall¹, J.T. Brown¹, F.A. Edwards⁸, D.A. Rusakov^{2,9}, M.G. Stewart⁵, and M.W. Jones^{1,+}

⁽¹⁾School of Physiology & Pharmacology, University of Bristol, University Walk, Bristol BS8 1TD, UK

⁽²⁾Department of Clinical and Experimental Epilepsy, UCL Institute of Neurology, University College London, Queen Square, London WC1N 3BG, UK

⁽³⁾Department of Neurodegenerative Disease, UCL Institute of Neurology, University College London, Queen Square, London WC1N 3BG, UK

⁽⁴⁾Institute of Cell Biophysics, Russian Academy of Sciences, Pushchino, Moscow Reg. 142290, Russia

⁽⁵⁾The Open University, Department of Life Sciences, Walton Hall, Milton Keynes, MK7 6AA, UK

⁽⁶⁾MRC National Institute for Medical Research, The Ridgeway, Mill Hill, London NW7 1AA, UK

⁽⁷⁾Department of Experimental Psychology, University of Oxford, Oxford OX1 3UD, UK

⁽⁸⁾Department of Neuroscience, Physiology and Pharmacology, University College London, Gower Street, London WC1E 6BT, UK

⁽⁹⁾Laboratory of Brain Microcircuits, Institute of Biology and Biomedicine, University of Nizhny Novgorod, Nizhny Novgorod 603950, Russia

These authors contributed equally to this work.

Abstract

Hippocampal pathology is likely to contribute to cognitive disability in Down syndrome (DS), yet the neural network basis of this pathology and its contributions to different facets of cognitive impairment remain unclear. Here, we report dysfunctional connectivity between dentate gyrus

Users may view, print, copy, and download text and data-mine the content in such documents, for the purposes of academic research, subject always to the full Conditions of use:http://www.nature.com/authors/editorial_policies/license.html#terms

*Correspondence to: Matt Jones, Ph.D. Matt.Jones@bristol.ac.uk.

Author Contributions

E.M.C.F. and V.L.J.T. designed the Tc1 mouse model and initiated the study. J.W., D.M.C. and A.T. performed extracellular *in vitro* electrophysiology and analyses; V.I.P. and I.K. performed EM and volumetric experiments and analyses; R.P. and T.P.J. performed two-photon imaging and intracellular electrophysiological recording and analyses; J.W. and L.E.Z. performed *in vivo* electrophysiology and analyses; S.J.L. performed behavioral experiments and analyses; J.T.B., A.D.R., D.B., F.A.E., M.G.S, D.A.R. and M.W.J. designed experiments, performed data analyses and wrote the paper.

*Sadly, Victor Popov died on 28th January, 2011

⁽¹⁰⁾Current address: University of Nebraska Medical Center, Omaha, NE 68198, U.S.A.

(DG) and CA3 networks in the transchromosomal Tc1 mouse model of DS, demonstrating that ultrastructural abnormalities and impaired short-term plasticity at DG-CA3 excitatory synapses culminate in impaired coding of novel spatial information in CA3 and CA1 and disrupted behaviour *in vivo*. These results highlight the vulnerability of DG-CA3 networks to aberrant human chromosome 21 gene expression, and delineate hippocampal circuit abnormalities likely to contribute to distinct cognitive phenotypes in DS.

Introduction

Down syndrome (DS) results from trisomy of human chromosome 21 (Hsa21) and is the most common genetically-defined cause of intellectual disability. However, the functions of many Hsa21 genes and the relative contributions of their over-expression to the diverse symptoms of DS remain undetermined. A range of aneuploid mouse models has been engineered to address this issue by linking trisomic over-expression of particular subsets of Hsa21 genes or their mouse orthologues to particular subsets of symptoms¹⁻³. Several of these mouse lines harbour hippocampal dysfunction and associated cognitive deficits, thereby corroborating clinical data suggesting that hippocampal abnormalities⁴⁻⁷ may be a root cause of some pre-dementia cognitive deficits – particularly in the realm of learning and memory – in DS patients^{8,9}.

Ts65Dn mice are the most widely studied DS model; they are partially trisomic for mouse chromosome 16 – which has a region of conserved synteny with Hsa21 – but their genetic basis in relation to DS is complicated by the trisomy of at least 60 non DS-related genes on mouse chromosome 17^{10, 11}. Ts65Dn mice display altered synaptic density, plasticity and excitatory-inhibitory balance in the hippocampus¹²⁻¹⁴ and abnormal synaptic morphology in DG and CA3^{15, 16}. However, the net impact of DG-CA3 dysfunction on *in vivo* hippocampal circuit function, information coding and output *via* CA1 in Ts65Dn mice has not been ascertained. The Tc1 ‘transchromosomal’ mouse line carries most of Hsa21 and is therefore a more direct model of trisomy 21. Tc1 mice also show phenotypic alterations in hippocampus-dependent behaviour and synaptic plasticity in DG, alongside cerebellar, cardiovascular and craniofacial traits reminiscent of human DS^{17, 18}. Taken together with findings in Ts65Dn mice, it therefore appears that DG and CA3 networks may be selectively vulnerable to changes in expression of Hsa21 genes or their mouse orthologues.

DG and CA3 abnormalities are likely to impact the routing, storage and recall of information involving pattern separation and completion¹⁹. This processing relies on feedback loops between the two subregions, which incorporate excitatory projections from DG granule cells (GC) to the autoassociative CA3 pyramidal cell network *via* mossy fibers (MF), GC MF projections to CA3 GABAergic interneurons and CA3-DG feedback *via* back-projections to GCs, DG interneurons and excitatory mossy cells of the hilus. The tuning of these circuits enables strong but selective excitation of subsets of CA3 pyramidal cells by specific GC assemblies. MF axons form low density, high efficacy excitatory synapses which target specialized postsynaptic structures known as thorny excrescences on CA3 pyramidal cells; these synapses are characterized by marked facilitation in response to repetitive GC firing at short latencies and can thereby act as ‘conditional detonator’ synapses, inducing

postsynaptic CA3 pyramidal cell spiking and consequent activation of connected CA1 cell ensembles only during particular patterns of GC activity²⁰.

Even subtle alterations of connectivity and excitatory-inhibitory balance in the DG-CA3 system are likely to confound accurate disambiguation or association of contextual (e.g. spatial) and temporal information during pattern separation and completion respectively, leading to impaired hippocampus-dependent episodic memory processing in DS and related diseases²¹. Using a combination of *in vitro* and *in vivo* imaging, electrophysiological and behavioral analyses, we show that overexpression of Hsa21 genes leads to ultrastructural and neurophysiological synaptic changes in DG and CA3 networks, and that consequent CA1 dysfunction contributes to cognitive impairment in the Tc1 mouse model of DS.

Results

Impaired mossy fiber short-term plasticity in Tc1 mice

To survey core features of hippocampal excitatory synaptic transmission in Tc1 mice, we recorded extracellular field potentials evoked by MF or Schaffer collateral stimulation in hippocampal slices from adult Tc1 mice and age-matched, wild-type littermates.

Baseline DG-CA3 transmission assessed using input-output curves was similar in Tc1 and wild-type mice (two-way mixed ANOVA, $F(1,19)=0.59$, $p=0.45$; Fig. 1a), as was DG granule cell excitability (Supplementary Fig. 1). However, a key physiological feature of MF transmission is pronounced short-term synaptic facilitation during repetitive stimulation; we investigated this phenomenon by delivering paired-pulse stimuli with inter-stimulus intervals (ISI) increasing logarithmically from 10-1000ms. MF field EPSPs from Tc1 and wild-type mice exhibited pronounced paired-pulse facilitation (PPF) at all ISIs tested, but PPF was consistently reduced (by 5-20%) in Tc1 mice relative to wild-type controls (two-way mixed ANOVA, $F(1,19)=7.02$, $p=0.02$; Fig. 1b). MF synapses also classically show marked frequency facilitation to trains of pre-synaptic stimuli delivered at ~1Hz. Synaptic facilitation during a 20 stimulus, 1Hz train was strongly attenuated in Tc1 mice compared to wild-type controls (two-way mixed ANOVA, $F(1,19)=10.99$, $p=0.004$; Fig. 1c), though the facilitation time constant was not different between the genotypes (wild-type= 3.04 ± 0.26 s, Tc1= 2.67 ± 0.31 s; unpaired t-test, $t(19)=0.88$, $p=0.39$).

In addition to MF short-term synaptic plasticity, we investigated NMDA receptor-independent long-term potentiation (LTP) at MF synapses in Tc1 and wild-type mice. LTP was induced using a 1s, 100Hz conditioning stimulus repeated 3 times at 10s intervals (Fig. 1d). At 25-30min post tetanisation we observed a stable LTP of $29.4\pm 11\%$ and $32.8\pm 8\%$ in wild-type and Tc1 mice respectively (unpaired t-test, $t(6)=-0.25$, $p=0.81$). DCG-IV (2μ) was applied at the end of experiments to confirm that responses were predominantly MF-driven (see Fig. 1d)²².

In contrast to MF-CA3 synapses, short-term plasticity (PPF) at Schaffer collateral synapses between CA3 and CA1 pyramidal cells remained intact in Tc1 mice and CA3-CA1 baseline transmission and LTP were also normal (Supplementary Fig. 2). Thus, whilst LTP appears intact in both CA3 and CA1, the short-term plasticity characteristic of MF-mediated

responses is preferentially impaired in Tc1 mice, consistent with preferential dysfunction of MF-CA3 transmission in the Tc1 model. This short-term facilitation is likely to play a central role in shaping the 'conditional detonator' properties of DG-CA3 connectivity, thereby tuning DG-CA3 interactions and downstream CA1 information processing during behavior.

Abnormal synapse density and ultrastructure in Tc1 mice

We used electron microscopy to characterize the structural underpinnings of hippocampal dysfunction in Tc1 mice, focusing on the DG-CA3 networks implicated by the brain slice electrophysiology described above. Hippocampus:brain volume ratios were normal in Tc1 mice relative to wild-type littermates (0.079 and 0.075 respectively; Supplementary Fig. 3a), suggesting gross hippocampal anatomy to be consistent between the two genotypes. Within DG of Tc1 mice, overall GC densities were normal (Supplementary Fig. 3b), as was general synaptic organisation of middle molecular layer (MML), where input from superficial layers of the entorhinal cortex (EC) forms excitatory synapses with GC dendritic spines. However, overall MML synapse density measured using 3-D reconstructions in a given tissue volume was significantly reduced in Tc1 mice (by 14.6%; $p=0.018$; Fig. 2a).

To establish whether the balance of MML synapse categories was altered in Tc1 mice, spines were classified as thin, stubby, mushroom or axo-dendritic according to their morphology and location. The proportions of all four subclasses of spines were normal in Tc1 mice (Fig. 2b). There were no statistically significant differences in volume or surface area of mushroom spines, the spine population that may represent mature synapses²³. However, 3-D reconstructions revealed that post-synaptic density (PSD) volumes of mushroom spines in the MML of Tc1 mice were significantly smaller than in wild-type ($0.014\pm 0.002\mu\text{m}^3$ vs. $0.021\pm 0.002\mu\text{m}^3$ respectively, $p=0.011$; Fig. 2c–e). Overall, these results suggest reduced input from EC to DG in Tc1 mice.

CA3 pyramidal cell densities were normal in Tc1 mice (Supplementary Fig. 3c). However, changes in CA3 synaptic architecture in Tc1 mice were more pronounced than in DG, with proximal apical dendrites of CA3 pyramidal cells showing a profound loss of postsynaptic thorny excrescences (compare serial sections Fig. 3a–d from wild-type with 3e–h from Tc1) particularly evident in 3-D reconstructions of CA3 dendritic segments (compare Fig. 3i with 3j; Supplementary Fig. 4). Thorn density was reduced from $3.8\pm 0.7\mu\text{m}^3$ in wild-type to $1.54\pm 0.32\mu\text{m}^3$ in Tc1 CA3; related effects on mossy fiber (MF) presynaptic giant boutons (GB) and PSDs are shown in Supplementary Fig. 4. Although average thorny excrescence volume was similar ($0.66\pm 0.13\mu\text{m}^3$ vs. $0.72\pm 0.10\mu\text{m}^3$ in wild-type and Tc1 respectively), the average volume of individual GB was markedly decreased in Tc1 mice (to $1.54\pm 0.32\mu\text{m}^3$ vs. $8.56\pm 2.48\mu\text{m}^3$ in wild-type). Similarly, Tc1 PSDs were smaller and less complex than in wild-type CA3 ($0.009\pm 0.002\mu\text{m}^3$ vs. $0.015\pm 0.002\mu\text{m}^3$ respectively).

The main ultrastructural differences between DG MF-CA3 synapses in Tc1 and wild-type mice are summarised schematically in Supplementary Fig. 5, and are likely to result in reduced direct excitation of CA3 pyramidal cells by input from DG GCs in the Tc1 DS model.

Imaging of mossy fiber input to CA3 pyramidal cells

To test whether perturbed synaptic connectivity in area CA3 of Tc1 mice could be detected in live cells, we examined fine dendritic structures in CA3 pyramidal cell dendrites using two-photon excitation imaging in acute hippocampal slices. Cells were held in whole-cell mode, loaded with a bright morphological tracer and showed robust synaptic responses throughout the experiments (see below and Methods). To minimize measurement bias, an unsupervised thresholding algorithm was used to calculate the maximum projection area of readily identifiable thorny excrescences per dendritic length in the first 15-20 μm of the primary apical dendrite and second-order dendrites next to the first bifurcation (Fig. 4a-d; Methods). Average thorny excrescence area per unit dendritic length for the primary apical dendrite was ~87% greater in wild-type compared to Tc1 CA3 pyramidal cells ($0.968\pm 0.147\mu\text{m}$ vs. $0.560\pm 0.065\mu\text{m}$; $n=15$ and 16 , respectively; unpaired t-test, $t(27)=3.07$, $p=0.011$; Fig. 4e). A similar, nearly two-fold difference was found in the second order dendrites next to the first bifurcation ($0.912\pm 0.08\mu\text{m}$ vs. $0.494\pm 0.049\mu\text{m}$, $n=23$ and $n=28$, respectively; $t(49)=4.64$, $p=2.67\text{e-}04$; Fig. 4e). These results confirm that ultrastructural synaptic abnormalities in Tc1 mice were not generated by the EM fixation process, and appear profound enough to impact DG-CA3 functionality.

Reduced MF input to CA3 pyramidal neurons in Tc1 mice

To test whether the functional MF input to CA3 pyramidal cells paralleled structural changes, we recorded miniature excitatory postsynaptic currents (mEPSCs) from CA3 pyramids (whole-cell mode, $V_m = -70\text{mV}$) in the presence of $1\mu\text{M}$ TTX. First, we measured the average overall frequency of mEPSCs as a basic indicator of the excitatory synaptic input and found no differences between Tc1 and wild-type slices ($n=11$ and 18 respectively; $p=0.843$). However, in addition to MF synapses, CA3 cells receive a powerful excitatory input from commissural fiber projections which might mask reductions in MF input. We therefore sought to measure the contribution of MF synapses by using a classical pharmacological dissection, suppressing MF release function with the group II metabotropic glutamate receptor (mGluR) agonist DCG-IV²².

As expected, applying $2\mu\text{M}$ DCG-IV for 15min to wild-type slices reduced the frequency of mEPSCs from $1.70\pm 0.4\text{Hz}$ to $0.37\pm 0.1\text{Hz}$ ($n=10$ cells from 8 mice; $t(9)=-6.58$, $p=1.01\text{e-}4$; Fig. 5a). In slices from Tc1 mice, this frequency was reduced by DCG-IV from $1.67\pm 0.4\text{Hz}$ to $0.69\pm 0.3\text{Hz}$ ($n=14$ cells from 9 mice; $t(13)=-4.71$, $p=4.07\text{e-}4$; Fig. 5b). We found that the average contribution of DCG-IV sensitive minis (attributable to the MF connectivity of CA3 pyramidal cells) was significantly lower in Tc1 than wild-type mice (wild-type $79.9\pm 3\%$ and Tc1 $59.0\pm 8.7\%$ of all minis, respectively; $t(22)=1.96$, $p=0.037$, non-equal variance t-test; Fig. 5c). This suggests that the relative weight of DG-CA3 synaptic connections (compared to commissural ones) in the Tc1 sample was significantly lower than in the wild-type. In addition, the variation of the DCG-IV effect among individual cells in the Tc1 mice was ~30% greater than in the wild-type ($p<0.005$, variance test). Indeed, one sub-group of sampled cells in the Tc1 mouse ($n=5$) showed a dramatically reduced effect of DCG-IV (Fig. 5c).

This bimodality in the Tc1 group of cells could be because Tc1 mice are mosaic for Hsa21, with different proportions of cells in different tissues carrying the additional chromosome; estimates of aneuploidy across whole brain range from 60–70%¹⁷. To test whether the uneven distribution of the DCG-IV sensitivity reflects this mosaicism at structural and functional levels, we examined the relationship between the frequency of DCG-IV-sensitive mEPSCs and the expression of thorny excrescences documented in the same cells. This analysis revealed that the thorny area per dendritic length was indeed positively correlated with the magnitude of the DCG-IV effect in the same cell ($n=7$, linear regression at $p=0.035$; Fig. 5d), thus establishing a relationship between morphological and functional cell phenotypes. These data provide evidence that Hsa21 aneuploidy resulted in reduced morphological and functional connectivity in the MF-CA3 pyramidal cell circuitry.

MF also project to GABAergic interneurons in CA3²⁴, raising the possibility that altered DG-CA3 connectivity in Tc1 mice may also impact inhibitory circuitry. To assess this, live MF axons in acute brain slices from 5 Tc1 and 5 wild-type mice were electroporated with fluorescent dye to allow two-photon imaging of MF-interneuron presynaptic terminals (Fig. 5e; Methods). These MF-interneuron connections are structurally distinguishable from the giant boutons synapsing on to pyramidal cells, appearing either as filopodia-like protrusions from MF giant boutons or as relatively small en-passant boutons in MF axons²⁵. We found that Tc1 and wild-type MF displayed similar anatomy, with similar numbers of detectable filopodial boutons (per giant bouton, $p=0.58$, rank sum test) and en-passant boutons (per unit length of MF axon, $p=0.75$) in both genotypes (Fig. 5f). These structural data indicate that DG-CA3 inhibitory connections appear unaltered relative to impaired excitatory connections in Tc1 mice.

Impaired place cell coding in CA3 and CA1 of Tc1 mice

Aberrant DG-CA3 synaptic morphology and short-term plasticity in Tc1 mice are likely to impact spatial information processing both within CA3 and, consequently, in downstream circuits in CA1. We therefore used implanted tetrodes to record either dorsal CA3 or CA1 place cell activity in freely-moving Tc1 and wild-type mice as they explored a novel, 80cm long linear track (Fig. 6). These behavioural conditions are likely to recruit entorhinal-hippocampal systems underpinning spatial learning and memory.

CA3 pyramidal cells in Tc1 (52 cells from 3 mice) and wild-type mice (47 cells from 3 mice) exhibited comparable mean firing rates (0.9 ± 0.1 and 1.1 ± 0.2 Hz respectively; $p=0.15$, rank sum test). However, CA3 pyramidal cell activity was more spatially diffuse in Tc1 mice, with Tc1 place cell spiking covering 29 ± 1.3 and wild-type spiking $25\pm 1.5\%$ of the linear track ($t(99)=-2.08$, $p=0.039$, unpaired t-test; Fig. 6e–g).

Larger place fields in the absence of higher firing rates may stem from trial-by-trial instability in firing locations; this effect has recently been demonstrated in CA1 of the Tg4510 mouse model of dementia²⁶, and in mice lacking functional NMDA receptors in CA1²⁷. Inter-trial spatial cross-correlations were slightly lower for Tc1 CA3 place cells (median [interquartile range] 0.059 [–0.02 to 0.14]) than wild-type place cells (0.071 [–0.01 to 0.27]; $p=0.049$, rank sum test; Fig. 6h), showing reduced stability of location-specific firing in Tc1 CA3, consistent with compromised input from upstream DG cell ensembles.

The activity of place cells is typically directionally sensitive on linear tracks, with firing rates conjunctively encoding both location and running direction. This directionality was quantified using a Directional Index (DI), defined as the magnitude of the difference between firing rates in the two directions, divided by the sum of the two firing rates. DI therefore ranges between 0 for place cells that fire at identical rates in the two directions, and 1 for cells that only fire in one of the two directions. In CA3, DI was similar for Tc1 (0.62 ± 0.04) and wild-type (0.60 ± 0.04) place cells ($t(97) = -0.31$, $p = 0.76$; Fig. 6i), indicating that at least some core features of CA3 spatial coding persist in Tc1 mice despite compromised DG input.

Aberrant CA3 place cell activity is likely to culminate in impaired spatial coding in CA1, where place cells are driven by convergent input from CA3 Schaffer collaterals and spatially modulated cells in the entorhinal cortex *via* the temporoammonic pathway. We isolated 50 Tc1 ($n = 7$ mice) and 63 wild-type ($n = 7$ mice) CA1 putative pyramidal cells (mean cluster Isolation Distances 19 ± 1.6 and 15 ± 1.1 for Tc1 and wild-type respectively; $p = 0.054$, unpaired t-test; see Fig. 6c–d for examples) during a single session on the linear track for each mouse.

Consistent with the *in vitro* data showing normal excitability in CA1 of Tc1 hippocampal slices, mean pyramidal cell firing rates on the track were similar in Tc1 mice and littermates (1.8 ± 0.2 and 1.6 ± 0.1 Hz respectively; $p = 0.55$, unpaired t-test), suggesting that overall CA1 excitability levels were not grossly affected by DG-CA3 changes. In line with our observations of CA3 place cell activity however, CA1 pyramidal cell firing was more spatially diffuse (median place field sizes, 36% [32 to 39] and 30% [21 to 36] for Tc1 and wild-type respectively; $p = 0.0003$, rank sum test; Fig 6g), and less stable from lap-to-lap in Tc1 mice (median inter-trial spatial cross-correlations, 0.044 [0.002 to 0.095] and 0.092 [0.001 to 0.29] for Tc1 and wild-type respectively; $p = 0.042$, rank sum test; Fig. 6h), suggesting that compromised CA3 place cell activity leads to downstream impairment in spatial coding in CA1 in Tc1 mice. Furthermore, DI for Tc1 CA1 place cells was 0.39 ± 0.04 , significantly lower than for wild-type (0.60 ± 0.03 ; $t(98) = 3.31$, $p = 0.0013$, unpaired t-test; Fig. 6i). Therefore, alongside reduced spatial selectivity and stability, Tc1 CA1 place cell firing rates discriminate running direction less accurately than CA1 place cells in wild-type mice.

Impaired hippocampus-dependent behaviour in Tc1 mice

Efficient spatial working memory performance (win-shift behaviour) on the radial arm maze requires the ability to distinguish accurately between similar reward arms and between different visits to those arms, and is thus likely to rely on effective pattern separation and completion and accurate spatial coding in place cell networks to disambiguate between overlapping events or episodes. This behaviour depends in part on DG function, since it is disrupted by deletion of the GluN1(NR1) subunit selectively from the GC of the DG²⁸, and was therefore chosen to probe DG-CA3-dependent behaviour in Tc1 mice under linear track-running conditions related to those used for place cell recordings.

Tc1 mice ($n = 9$) were slower than wild-type littermates ($n = 11$) to attain an efficient level of spatial working memory performance on the radial maze task, with a significant main effect of block ($F(3,54) = 56.20$; $p = 1e-4$) and, importantly, a significant genotype-by-block

interaction (Fig. 7; $F(3,54)=3.36$; $p=0.025$; Methods). This was independent of the age at which the animals were tested (all interactions $p>0.20$; although overall performance was poorer in older animals – $F(1,18)=8.18$; $p=0.01$). Further investigation of the genotype-by-block interaction using analysis of simple main effects revealed that spatial working memory performance in the Tc1 mice was significantly impaired during the second block of testing ($F(1,18)=10.78$; $p=0.004$). There was also a non-significant trend towards impaired performance in block 3 ($F(1,18)=2.96$; $p=0.10$), but by block 4 Tc1 performance was similar to that of wild-type animals ($F(1,18)=0.134$; $p=0.72$).

To control for the possibility that differences in spatial working memory performance were due to differences in running speed (animals that run more slowly may experience a longer delay between choices, and thus experience a greater mnemonic demand), running times were recorded during trials 14-16 of the second training block. The total time to complete the trial and collect all 6 rewards was recorded and divided by the total number of arm choices made, giving a measure of performance speed in terms of time per choice. The performance speeds did not differ between groups (median [IQ range]: wild-type=26.0s [22.3–28.9], Tc1=28.0s [27.8–33.4], $p=0.07$, rank sum test). Spatial working memory performance (choice accuracy) was impaired in the Tc1 mice during these trials (Errors per trial: wild-type= 0.42 ± 0.12 , Tc1= 1.44 ± 0.52 ; $t(18)=2.10$; $p=0.05$).

These behavioural data therefore corroborate conclusions from structural and neurophysiological studies of DG, CA3 and CA1 in the Tc1 mouse model of DS, showing that impaired activity and interactions in these hippocampal subfields culminate in cognitive dysfunction associated with over-expression of Hsa21 genes.

Discussion

Our ultrastructural analyses of DG MML and proximal dendrites of CA3 pyramidal cells in both fixed tissue and living cells reveal synapse loss and altered spine morphology in Tc1 mice strikingly reminiscent of that reported in the Ts65Dn mouse model of DS¹⁶; this implicates altered expression of genes common to both models in triggering hippocampal abnormalities. Additional DS mouse models include Ts1Cje and Ts1Rhr mice, the latter being trisomic for only a ‘Down Syndrome Critical’ subset of mouse genes triplicated in both Ts65Dn and Ts1Cje²⁹. Since the reduction of MML synapse density appears common to Tc1, Ts65Dn and Ts1Rhr models, conserved syntenic regions of Mmu16 and Hsa21 may trigger this DG phenotype. Specific candidate genes include the dual-specificity protein kinase Dyrk1A, which is increasingly implicated in Alzheimer’s Disease (AD)-related pathology in DS³⁰. However, since Tc1 mice unexpectedly fail to over-express human amyloid precursor protein (APP), the synaptic abnormalities described here can be categorically dissociated from A β -associated neurodegeneration. Tc1 mice therefore recapitulate hippocampal dendritic spine abnormalities seen in DS sufferers prior to onset of AD³¹ and present a unique opportunity to distinguish between DS and AD-related phenotypes.

Reduced DG MML synapse density, smaller PSD volumes and reduced presence of postsynaptic thorny excrescences are likely to underlie the reduced surface expression of the

AMPA receptor subunit GluR1 seen in Tc1 mice¹⁸, presumably resulting in reduced excitatory synaptic drive of GCs by entorhinal cortical (EC) afferents *via* the medial perforant pathway. Despite this, we found no evidence for a compensatory increase in GC intrinsic excitability (Supplementary Fig. 1). The smaller mushroom spine PSDs in Tc1 mice are also consistent with attenuation of synaptic plasticity-induced synaptic enlargement²³, and may reflect the attenuated perforant path plasticity evident in Tc1 mice^{17, 18}. Plasticity at perforant path-GC synapses is required for normal DG function, for example underpinning pattern separation³². Thus, EC input to DG in this mouse model of DS appears severely compromised, and is presumably a critical contributor to impaired CA3 and CA1 place cell function in Tc1 mice.

Behavioral data suggest that Tc1 hippocampal circuit abnormalities manifest preferentially during periods of enhanced demand for spatial memory processing: To date, Tc1 mice have been reported to show normal learning in a standard version of the watermaze and normal spontaneous alternation in a T-maze¹⁷, a rule- and reinforcement-free test of innate behavior, but show significant impairments in the 6-arm radial arm maze task used here. This is consistent with impaired pattern separation and preferential retardation of more complex cognitive processing during conditions that necessitate disambiguation of multiple rewarded locations and/or episodes and may therefore necessitate enhanced EC-DG recruitment. Further testing is required to determine whether Tc1 behavioral impairments also reflect load-dependent visuospatial working memory deficits, a phenotype observed in DS patients³³. However, alongside evidence for DG hypocellularity in DS³⁴, over-inhibition of DG in Ts65Dn mice¹³, and impaired DG-dependent behaviour in the Ts65Dn model³⁵, our study indicates that attenuated EC-DG synaptic function may be a central contributor to intellectual disabilities stemming from pattern separation failures. Whether or not direct EC input to CA1 *via* the temporoammonic pathway is also compromised in DS or DS models remains to be tested. It may be that unreliable spatial coding in CA1 of Tc1 mice stems from disrupted input from both the DG-CA3 network and temporoammonic pathway, creating a 'mis-match' between inputs from CA3 place cells and spatially modulated cells in EC (i.e. grid cells, border cells and head direction cells) during memory-guided behaviour.

Different components of hippocampus-dependent information processing cannot be categorically assigned to single hippocampal subfields, and the trade-off between pattern separation and completion is mediated by the DG and its interactions with CA3^{19, 36}. Reduced synaptic drive of DG might be expected to lead to reduced downstream activation of CA3 in Tc1 mice, particularly when combined with the profound reduction in the number and complexity of MF-CA3 pyramidal cell excitatory synapses evident at the EM level. Our patch clamp recordings clearly demonstrate reduced MF input to individual CA3 pyramidal cells of Tc1 mice *in vitro*, since (1) they showed a smaller proportion of MF-associated miniature excitatory events and (2) CA3 pyramidal cells with reduced thorny excrescence volume (potentially those carrying Hsa21, since Tc1 mice are mosaic for the transchromosome) showed a correlated reduced drive by MF. These analyses point to attenuated DG-CA3 interactions as a central component of hippocampal dysfunction in Tc1 mice.

In addition to reduced basal levels of MF input, our data show an impairment of MF short-term synaptic facilitation in Tc1 mice. This form of short-term plasticity is triggered by mechanisms dependent upon presynaptic Ca^{2+} concentration; its impairment may therefore reflect the reduced MF giant bouton volume shown here in Tc1 mice, though the abnormal postsynaptic excrescences may also contribute. The fact that NMDA receptor-independent LTP at MF synapses appeared intact in Tc1 mice (as it does in organotypic slices from the Ts65Dn mouse model of DS³⁷) supports the notion that Ca^{2+} from different sources may trigger the two forms of plasticity²², which may in turn make differential contributions to information processing. Nevertheless, attenuated MF short-term plasticity is likely to detract from 'detonator synapse' function and exacerbate impaired information transfer across DG, CA3 and CA1 networks in Tc1 mice. A similar deficit in MF short-term potentiation has been identified in a transgenic mouse model of Alzheimer's disease³⁸, hence this phenotype may be more widely distributed in conditions associated with cognitive impairment.

DS is a systemic disease, and its cognitive symptoms are unlikely to stem solely from hippocampal dysfunction. Nevertheless, the central roles of the hippocampus in rapidly and accurately encoding, integrating or retrieving components of episodic memory do mean that any reduced or aberrant connectivity in hippocampal circuits is likely to prove disproportionately disruptive, particularly if present throughout the lifespan as appears to be the case in DS⁴⁻⁷. Abnormalities in DG and CA3 may be particularly disruptive, since their precisely connected and dynamically tuned networks act together to filter and associate information during mnemonic processing¹⁹. Commonalities across aneuploid mouse models of DS now point to over-expression of a subset of Hsa21 genes (not including APP, responsible for AD-related neurodegeneration) driving a combination of reduced EC input to DG, abnormal DG-CA3 connectivity and consequently impaired information processing in CA3 and CA1 networks. These abnormalities are likely to preferentially impair cognition dependent upon pattern separation and completion (e.g. disambiguation between overlapping/competing memories), and cognitive testing in patients should be used to test this explicitly.

Finally, the impact of potential pharmacological therapies for cognition in DS³⁹ on DG-CA3-CA1 interactions should also be re-considered: the network effects of targeting one hippocampal subfield (for example normalisation of reduced inhibition in DG⁴⁰) must be taken into account, and therapeutic approaches based on AD-associated cognitive impairments⁴¹ may not be well-suited to treatment of pre-dementia DS. That said, potential pharmacological or behavioral therapies impacting DG neurogenesis^{42, 43} may go some way to re-balancing the entorhinal-hippocampal networks that this study of Tc1 mice implicates as central to hippocampal abnormalities in DS.

Methods

Animals

Experiments were performed in accordance with the UK Home Office Animals (Scientific Procedures) Act (1986) and institutional Ethical Committee guidelines. The transchromosomal mouse line Tc1 was generated as described elsewhere¹⁷. This trans-species aneuploid mouse line stably transmits a freely segregating, almost complete copy of

Hsa21 in a C57BL/6J_129S8 (F2) genetic background. Tc1 and their wild-type littermates are obtained from the mating of C57BL/6J_129S8 (F1) Tc1 females with C57BL/6J_129S8 (F1) males. Animals were genotyped by PCR, weaned at 3 weeks and housed by gender and litter under standard conditions. Experiments were conducted on adult male (6–14 months old) mice during the light phase of a 12-h light/dark schedule (with lights on at 7.00 A.M.) unless stated otherwise.

Histology and electron microscopy

Mice were anaesthetised with sodium pentobarbital (100mg/kg, i.p.) and transcardially perfused with 0.5% glutaraldehyde and 2.0% paraformaldehyde. For volume estimates, 50µm coronal sections were taken using Leica vibratome and every fifth section mounted on gelatine coated glass slides and stained using Toluidine Blue (0.5% for 1min). Sections were dehydrated and mounted with DPX under cover glass and JPEG mages were captured under a X1 objective. Full-field JPEG images were aligned and the contours of each section of brain and hippocampal region traced digitally and volumes computed.

For EM, coronal vibratome hippocampal sections (50µm in thick) were cut and fixed further by immersion in 0.1M Na-cacodylate buffer (pH 7.2–7.3) containing 2.5% glutaraldehyde for 1–2h at room temperature, followed by three washes in 0.1M Na-cacodylate buffer. Tissue was post-fixed with 1% osmium tetroxide and 0.01% potassium dichromate in 0.1M Nacacodylate buffer for 1–1.5h at room temperature. Serial sections were cut with a Diatome diamond knife forming a ribbon of 800-1000 serial sections in the knife bath. These were broken into series of 15-20 sections, collected on pioloform-coated slot grids and counterstained with saturated ethanolic uranyl acetate followed by Reynolds lead citrate. The series were examined with a JEOL 1010 electron microscope and photographed at 6,000-10,000x magnification. Cross-sectioned axons, dendrites, and mitochondria spanning all sections provided a reference for initial alignment of serial sections. Section thickness was determined using the approach of Fiala and Harris⁴⁴.

Digitally scanned EM negatives (900 dpi) were aligned as JPEG images (software available from Drs. Fiala and Harris, <http://synapses.clm.utexas.edu/>). Alignments were made with full-field images. Contours of individual cells and their elements were traced digitally and computed to enable 3-dimensional reconstructions. For synapse density analysis, 4 mice per group were analysed with 1 series of 50 sections per animal, (~30µm³ of tissue for each). Analyses of variance (ANOVAs) followed by Bonferroni's or Tukey's unequal N honest significant differences tests were performed with Origin 7.0 (Northampton, MA). Data are presented as mean ± SEM.

In vitro electrophysiology

Preparation 1: two-photon excitation imaging and whole-cell recording—Acute hippocampal slices 280µm thick were obtained from 6-10 week old male Tc1 mice and wild-type littermates. Slices were prepared in ice-cold slicing solution containing (in mM): NaCl 60, sucrose 105, KCl 2.5, MgCl₂ 7, NaH₂PO₄ 1.25, NaHCO₃ 26, CaCl₂ 0.5, ascorbic acid 1.3, sodium pyruvate 3 and glucose 8 (osmolarity 300-310 mOsM), stored in slicing solution at 34°C for 20 minutes before being transferred to an interface chamber for storage

in extracellular solution containing (in mM) NaCl 119, KCl 2.5, MgSO₄ 1.3, NaH₂PO₄ 1, NaHCO₃ 26, CaCl₂ 2, glucose 20 (osmolarity adjusted to 295-305 mOsM with glucose). All solutions were bubbled continuously with 95% O₂/5% CO₂. Slices were allowed to rest for at least 60min before recordings started. For recording, slices were transferred to the submersion-type recording chamber and superfused, at room temperature (22-24°C) with artificial cerebrospinal fluid saturated with 95% O₂/5% CO₂ containing (in mM): NaCl 119, KCl 2.5, NaH₂PO₄ 1, CaCl₂ 2, MgSO₄ 1.3, NaHCO₃ 26, glucose 20 (pH 7.4; osmolarity 295–305 mOsM).

Electrophysiology—Whole-cell recordings in CA3 pyramidal neurons were performed using 3-3.5 MΩ pipettes with an intracellular solution (in mM): K Gluconate 130, KCl 5, MgCl₂ 2, HEPES 10, di-tris-Phosphocreatine 10, NaATP 4, NaGTP 0.4 (pH adjusted to 7.2 with KOH, osmolarity 290-295 mOsM). The morphological tracer Alexa Flour 594 hydrazide (50μM) was also included in the intracellular solution. Voltage clamp recordings of miniature EPSCs were made, with the mEPSCs recorded at -70 mV. Receptor agonists and antagonists purchased from Tocris Cookson (Bristol, UK) were added to the aCSF at the following concentrations (in μM): TTX 1, Picrotoxin 100 and DCG-1V ((2S, 2'R, 3'R)-2-(2', 3'-dicarboxycyclopropyl) glycine) 2. Recordings were performed with a Multiclamp 700B amplified (Molecular Devices). Recording sweeps were collected at 5kHz using WinWCP (Strathclyde Electrophysiology). mEPSCs were recorded over 15min periods in control and treated conditions, data were then analyzed off-line using Mini-Analysis software (Synaptosoft). mEPSCs were detected if their amplitude was greater than the threshold of 5pA, and considered for analysis if their rise time was shorter than their decay time. Fluorescent probes were purchased from Invitrogen.

Two-photon excitation fluorescence imaging—We used a Radiance 2000 imaging system (Zeiss-Bio-rad) or Olympus Fluoview imaging system optically linked to a femtosecond pulse laser Mai-Tai (Spectraphysics-Newport) and integrated with patchclamp electrophysiology. CA3 pyramidal cells loaded with 50μM Alexa Fluor 594 were imaged as stacks of 30-60 optical sections in the Alexa emission channel (λ_{2P_x} =800nm), collected in image frame mode (512 pixels x 512 pixels, 8-bit) at 0.5μm steps (Fig. 4). To minimize any measurement bias, we calculated the visible (maximum projection) area of the identifiable thorny excrescences per dendritic length in the first 15-20 μm of (a) the primary apical dendrite and (b) second-order dendrites next to the first bifurcation using an unsupervised thresholding algorithm. The algorithm divides the image into objects and background by initiating a test threshold and computing the average of the pixels at or below the threshold and pixels above. It then computes the average of those two, increments the threshold, and repeats the process until threshold = (average background + average objects)/2. For figure illustration purposes, the image stacks were z-axis averaged with ImageJ routines (Wayne Rasband, ImageJ, National Institute of Health).

Visualisation of live Mossy Fiber Boutons by axonal electroporation of fluorescent tracer dyes—To visualise the morphology of mossy fiber giant boutons in acute hippocampal slice preparations, a modification of the electroporation method originally described by Neviau and Helmchen (2007)⁴⁵ was developed. As opposed to

electroporating individual dentate granule cells with fluorescent dyes and tracing the axons to CA3, mossy fiber axons in CA3 *Stratum Lucidum* were directly loaded by electroporation. Slices were prepared and maintained as per Preparation 1. The mossy fiber tract was routinely identified under DIC and a monopolar glass stimulating electrode (4–5M Ω tip resistance) filled with intracellular solution supplemented with 1mM Alexa 594 (to highlight the morphology of labelled boutons) and 1mM of the Ca²⁺ sensitive dye Fluo-5F (to assess their *viability*) was positioned with the tip at a 45–90° angle to the edge of the tract facing toward the pyramidal cell layer. Once positioned, a 100ms duration -10V electroporation pulse was delivered through a constant voltage stimulus isolation box (Digitimer, Welwyn Garden City, UK); multiple electroporation sites were used per slice until one or more MF boutons could be readily imaged. Boutons displaying morphology as observed in whole cell patch loaded granule cells⁴⁶ with little fluorescence in the Fluo 5F channel indicating a low basal [Ca²⁺]_i were accepted for further investigation. Bouton morphology was imaged in frame scan mode as a stack of 30–60 frames taken in 0.25 μ m steps, with a size of 512 x 512 pixels and a pixel size of 0.05 μ m. Numbers of en passant and filopodial axonal boutons were then counted using 3D stacks of images by the experimenter whom was blinded to genotype until analysis was complete. Morphological criteria for bouton identification were consistent with detailed 3D reconstructions in fixed preparations²⁶ and with previous reports of live Alexa-filled MFs in acute slices⁴⁶.

Preparation 2: MF-CA3 field potential recordings—500 μ m transverse hippocampal slices were prepared from male, 5–7 month old Tc1 mice and wild-type littermate controls (mean 6 months). Briefly, animals were killed *via* cervical dislocation, the brain rapidly removed and placed into ice cold, high sucrose solution containing (in mM): sucrose 189, glucose 10, NaHCO₃ 26, KCl 3, MgSO₄.7H₂O 5, CaCl₂ 0.1, NaH₂PO₄ 1.25 (osmolarity 295–305 mOsM). The cerebellum and frontal cortex were removed and the brain was separated into the two hemispheres. The hippocampus was then removed from each hemisphere and sliced along its transverse axis in ice-cold high sucrose solution. Slices were stored in a submerged incubation chamber at 37°C for 30min and then at room temperature in aCSF containing (in mM): Glucose 10, NaCl 124, KCl 3, NaHCO₃ 24, NaH₂PO₄ 1.25, MgSO₄.7H₂O 1, CaCl₂ 2 (osmolarity 295–305 mOsM). All solutions were continuously bubbled with 95% O₂/5% CO₂. Slices were allowed to rest for at least 60min before recordings were made. For recording, slices were transferred to an interface-type recording chamber and superfused at 33±1°C with aCSF saturated with 95% O₂/5% CO₂.

Electrophysiology—Extracellular recordings were made from *stratum lucidum* using glass micropipettes (~3M Ω) filled with aCSF. Mossy fiber (MF) field EPSPs were evoked by 100 μ s electrical stimulation of the dentate gyrus granule cell layer using a concentric bipolar stimulating electrode (Inner diameter 12.5 μ m; Royem Scientific Ltd, Luton, UK) connected to an isolated stimulator box (Digitimer, Welwyn Garden City, UK). To determine the maximal MF fEPSP, we delivered a saturating 300 μ A pulse. Subsequent stimuli were then delivered at the current capable of inducing half of the maximum response.

Short-term MF synaptic plasticity was investigated in two ways: first, we recorded paired-pulses delivered over a range of inter-stimulus intervals varying logarithmically over two orders of magnitude (10–1000ms); secondly, we measured the change in synaptic response to a 20 pulse, 1Hz stimulus train. MF long-term potentiation (LTP) experiments were performed in the presence of 5 μ M L689,560 (Tocris Cookson, Bristol, U.K.) to block NMDA receptor function. Baseline synaptic transmission was recorded to stimuli delivered every 30s for at least 10min. NMDA receptor-independent LTP was then induced by a conditioning stimulus consisting of a 1s, 100Hz train, repeated 3 times at 10s intervals. LTP was followed for 30min post tetanisation.

Recordings were made using an AxoClamp2B amplifier (Scientifica, Uckfield, U.K.) in series with a secondary instrumentation amplifier (NPI, Tamm, Germany). Signals were amplified 2000 times, low pass filtered at 10kHz and sampled at 50kHz using Clampex 10.1 software (Molecular Devices). fEPSPs were confirmed as arising from MFs by bath application of 2 μ M DCG-IV (Tocris Cookson); only fEPSPs reduced by 70% after 20min DCG-IV application were included in analyses. Excitability of DG GCs was characterized by extracellularly recording compound action potentials (CAP) in the GC layer of DG in response to antidromic activation of MFs by stimulation in area CA3; these experiments were performed in the presence of the AMPA/Kainate receptor antagonist NBQX (5 μ M).

Data were analysed off-line using Clampfit 10.1 (Molecular Devices). The maximum amplitude of the MF fEPSP was measured. N-numbers refer to experiments performed on a single slice taken from an individual animal. The Student's repeated measures t-test and repeated measures two-way ANOVA were used to test for significance where appropriate.

Preparation 3 – Schaffer collateral-CA1 field potential recordings—For CA3–CA1 synaptic recordings, 400 μ m transverse hippocampal slices were prepared from 9–12 week old Tc1 mice and wild-type littermate controls. Animals were killed by decapitation, the brain rapidly removed to ice cold slicing medium, containing (in mM): 125 NaCl, 2.4 KCl, 26 NaHCO₃, 1.4 NaH₂PO₄, 20 D-glucose, 3 MgCl₂, 0.5 CaCl₂, ~315 mOsm/l. Slices were subsequently transferred at 5 minute intervals to medium containing gradually more-physiological Ca²⁺ and Mg²⁺ concentrations (in mM Ca²⁺/Mg²⁺): (0.5/3; 0.5/1; 1/1; 2/1), maintained at 36°C and saturated with 95% O₂/5% CO₂. Finally, slices were left to recover for >40 minutes in a submerged incubation chamber at room temperature. For recording, slices were transferred to a submerged recording chamber and superfused with saturated aCSF (as slicing medium, with 2mM Ca²⁺ and 1mM Mg²⁺, saturated with 95% O₂/5% CO₂ and maintained at 30 \pm 1°C).

Electrophysiology—Extracellular field recordings were made from *stratum radiatum* using glass micropipettes (~1.5M Ω), filled with aCSF. Electrical stimulation was applied to Schaffer collateral fibers at 0.1Hz via a glass stimulating electrode filled with aCSF placed in the *stratum radiatum* either anterograde or retrograde to the recording electrode and connected to an isolated constant voltage (100 μ s) stimulator (Digitimer, UK). To determine the maximal fEPSP, a stimulus-response relationship was evoked between 10–80V and subsequent stimulation intensity set at the lower intensity of either 30–50% maximum response, or 30–50% of the threshold for a population spike. Long-term synaptic plasticity

was examined by applying a tetanic stimulation, consisting of a 200ms 100Hz train, repeated 3 times at 1.5s intervals. LTP was followed for 1hr post conditioning.

Recordings were made using an AxoClamp 2B amplifier (Molecular Devices, CA, USA) with an HS-2A x1 headstage. 10Vm output signals were filtered at 10kHz and subsequently amplified 100 times and low-pass filtered at 2kHz (Frequency Devices 900 Filter) and then sampled at 10kHz *via* an ITC16 digitizer connected to WinWCP software (Strathclyde Electrophysiology). fEPSP slope was measured from an average of 6 responses using the linear function within the Curve-Fit Analysis of WinWCP.

In vivo electrophysiology

Tetrode implants and surgery—10 wild-type and 10 Tc1 male mice (4–8 months; 3 of each genotype for CA3 recordings, 7 of each for CA1) were implanted with 4–6-tetrode microdrives over the right dorsal hippocampus (centred 2.5mm posterior and 2.3mm lateral from bregma for CA3, 1.5mm lateral for CA1) under aseptic conditions and ketamine/xylozine recovery anesthesia. Each tetrode was spun from polyimide-insulated 13 μ m nichrome wire (Kanthal, Hallstahammarm, Sweden). Drives were attached to the skull using gentamicin-impregnated Palacos[®] R-40 cement and 4 stainless steel skull screws, one of which (over cerebellum) served as a ground connection for recording. After surgery, mice were individually housed with *ad libitum* access to food and water.

During the 7–20 days following surgery, the independently moveable tetrodes were lowered into either the CA3 or CA1 pyramidal cell layer (identified by the characteristic burst firing of single-units and the presence of ripple or sharp-wave ripple events in local field potential) while mice occupied a small (15x15cm base) holding box, set to one side of the linear track subsequently used for place cell recordings (see below). Extracellular action potentials (sampled at 30kHz and filtered between 0.6–6kHz) were recorded differentially *via* a unity gain HS-18 preamplifier and Digital Lynx (Neuralynx, MT) using local references. In a subset of mice, tetrode tip positions were verified post mortem.

Recording setup—Recordings were made on an 80cm long, 5cm wide linear track with open 9cm high walls and a turning zone (10 x 10cm) at each end, located in the middle of a room. All data were recorded during each mouse's first, novel exposure to the track. The linear track was made from dark grey plastic. Half of the white room walls were exposed and half covered by a black curtain; 3-D cardboard cues were hung to create a distinct spatial context. Eight regularly spaced incandescent bulbs were hung overhead to dimly illuminate the room. Video tracking sampled the positions of green and red LEDs attached to the preamplifier at 60Hz, with a final resolution of approximately 1.5cm.

Tetrode data analysis—All analyses were performed blind to genotype in MATLAB (MathWorks, MA). Spikes were sorted semi-automatically on the basis of waveform characteristics (amplitude and energy) using KlustaKwik (K.D. Harris, <http://klustakwik.sourceforge.net/>), and clusters were then refined manually with MClust in MATLAB (A.D. Redish, <http://redishlab.neuroscience.umn.edu>). Only units with less than 1% of inter-spike intervals below 2ms and cluster isolation distances above 10 were selected for further analysis⁴⁷; cells with mean firing rates between 0.1 and 5Hz on the linear track

were considered putative pyramidal cells. Trial-by-trial positional firing correlations were calculated as described by Cheng and Ji (2013)²⁶, using 4cm positional bins and excluding the turning zones at each end of the track; only cells with firing rates of at least 0.1Hz in both running directions were included in this trial-by-trial analysis, with trials that took longer than 20s excluded. The extent of spatial firing was based on firing rate maps on the linear track³².

Radial arm maze

This study employed precisely the same maze, housed in the same facility as that used by Niewoehner et al. to demonstrate the dependence of task performance on normal DG function²⁷.

Wild-type (n=11) and Tc1 (n=9) mice were trained on a spatial working memory version of the radial maze task. Mice were first habituated to drinking a sweetened, condensed milk reward in their home cages, then habituated to drinking milk on an elevated Y-maze in their colony holding room (*i.e.* not the room used for spatial memory testing). The Y-maze consisted of three identical wooden arms, each 50cm long by 9cm wide, with a low white plastic wall (0.5cm), connected by a central polygonal platform (14cm diameter). The maze was painted black. A food well was positioned at the end of each arm.

The radial maze was made of wood and painted grey. It consisted of six arms (60cm x 7cm) radiating out from a central platform. Each arm was surrounded by a 1cm raised edge and contained a food well located at the end. The central platform was surrounded by a transparent Perspex cylinder (18cm diameter, 30cm high). At the entrance to each arm, a Perspex door (6cm wide, 7cm high) could be controlled manually by the experimenter using a series of strings. The maze was positioned 80cm above the floor and was surrounded by prominent distal extramaze cues.

To specifically assess hippocampus-dependent, spatial working memory, all six arms were baited with 0.05ml sweetened condensed milk. At the start of each trial, the mouse was placed on the central platform and given a free choice of arms. After visiting the food well in the chosen arm and consuming the milk reward, the mouse would return to the central platform. Doors were used to contain the animals on the central platform between choices and thus prevent the use of simple mediating strategies. After 10s, all doors were then re-opened and the mouse allowed another choice. This was repeated until the mouse had visited all of the baited arms. Each entry into an arm that had previously been visited on that trial (and was now un-baited) was scored as a spatial working memory error.

Mice received 1 trial per day for a total of 24 days. Each mouse was tested twice: first at an age of 5-6 months and then again at 18 months of age. Data were collected in 6 trial blocks for analysis.

Statistical analyses

Data sets were tested for normality and parametric or non-parametric, two-sided tests used as appropriate with an α level of 0.05. Where appropriate, two-way analysis of variance (ANOVA) was used to compare datasets across multiple factors. Post-hoc comparisons were

made using a Bonferonni correction for multiple comparisons. Sample sizes were not formally predetermined using power calculations, but are consistent with previous studies combining *in vitro*, *in vivo* and behavioural measures³² and designed to enable detection of at least a 15% difference in the population mean at a $p < 0.05$ level given the sampled population variance. Imaging and electrophysiological data were collected from Tc1 and WT mice in randomized order and quantified blind to genotype. The majority of data are presented as mean \pm SEM; where medians are presented for non-normally distributed data, the inter-quartile range is given in square brackets (median [IQR]).

Supplementary Material

Refer to Web version on PubMed Central for supplementary material.

Acknowledgements

Thanks to The Wellcome Trust (Programme Grant to E.M.C.F., V.L.J.T. and M.W.J., Principal Fellowship to D.A.R.), the Medical Research Council (grant to E.M.C.F. and V.L.J.T., Industrial Collaborative Studentship to J.W.), ERC Advanced Grant and FP7 ITN Extrabrain (D.A.R.), and The Russian Foundation for Basic Research (Grants 15-1430000 to D.A.R. and 08-04-00049a to V.I.P.) for financial support, and to Amy Slender, Heather Davies and Debi Ford for expert technical assistance.

References

1. Reeves RH, et al. A mouse model for Down syndrome exhibits learning and behaviour deficits. *Nature Genetics*. 1995; 11:177–184. [PubMed: 7550346]
2. Yu T, et al. A mouse model of Down syndrome trisomic for all human chromosome 21 syntenic regions. *Hum. Mol. Genet*. 2010; 19:2780–2791. [PubMed: 20442137]
3. Pereira PL, et al. A new mouse model for the trisomy of the Abcg1-U2af1 region reveals the complexity of the combinatorial genetic code of down syndrome. *Hum. Mol. Genet*. 2009; 18:4756–4769. [PubMed: 19783846]
4. Kesslak JP, Nagata SF, Lott I, Nalcioglu O. Magnetic resonance imaging analysis of age-related changes in the brains of individuals with Down's syndrome. *Neurology*. 1994; 44:1039–1045. [PubMed: 8208396]
5. Raz N, et al. Selective neuroanatomic abnormalities in Down's syndrome and their cognitive correlates: evidence from MRI morphometry. *Neurology*. 1995; 45:356–366. [PubMed: 7854539]
6. Aylward EH, et al. MRI volumes of the hippocampus and amygdala in adults with Down's syndrome with and without dementia. *Am. J. Psychiatry*. 1999; 156:564–568. [PubMed: 10200735]
7. Pinter JD, Eliez S, Schmitt JE, Capone GT, Reiss AL. Neuroanatomy of Down's syndrome: a high-resolution MRI study. *Am. J. Psychiatry*. 2001; 158:1659–1665. [PubMed: 11578999]
8. Pennington BF, Moon J, Edgin J, Stedron J, Nadel L. The neuropsychology of Down syndrome: evidence for hippocampal dysfunction. *Child Devel*. 2003; 74:75–93. [PubMed: 12625437]
9. Edgin JO, et al. Development and validation of the Arizona Cognitive Test Battery for Down syndrome. *J. Neurodevelop. Disord*. 2010; 2:149–164.
10. Duchon A, et al. Identification of the translocation breakpoints in the Ts65Dn and Ts1Cje mouse lines: relevance for modeling Down syndrome. *Mammalian Genome*. 2011; 22:674–684. [PubMed: 21953411]
11. Reinholdt LG, et al. Molecular characterization of the translocation breakpoints in the Down syndrome mouse model Ts65Dn. *Mammalian Genome*. 2011; 22:685–691. [PubMed: 21953412]
12. Kurt MA, Kafa MI, Dierssen M, Davies DC. Deficits of neuronal density in CA1 and synaptic density in the dentate gyrus, CA3 and CA1, in a mouse model of Down syndrome. *Brain. Res*. 2004; 1022:101–109. [PubMed: 15353219]

13. Kleschevnikov AM, et al. Hippocampal long-term potentiation suppressed by increased inhibition in the Ts65Dn mouse, a genetic model of Down syndrome. *J. Neurosci.* 2004; 24:8153–8160. [PubMed: 15371516]
14. Belichenko PV, et al. Excitatory-inhibitory relationship in the fascia dentata in the Ts65Dn mouse model of Down syndrome. *J. Comp. Neurol.* 2009; 512:453–466. [PubMed: 19034952]
15. Belichenko PV, et al. Synaptic structural abnormalities in the Ts65Dn mouse model of Down Syndrome. *J. Comp. Neurol.* 2004; 480:281–298. [PubMed: 15515178]
16. Popov VI, Kleschevnikov AM, Klimenko OA, Stewart MG, Belichenko PV. Three-dimensional synaptic ultrastructure in the dentate gyrus and hippocampal area CA3 in the Ts65Dn mouse model of Down syndrome. *J. Comp. Neurol.* 2010; 519:1338–1354. [PubMed: 21452200]
17. O'Doherty A, et al. An aneuploid mouse strain carrying human chromosome 21 with Down syndrome phenotypes. *Science.* 2005; 309:2033–2037. [PubMed: 16179473]
18. Morice E, et al. Preservation of long-term memory and synaptic plasticity despite short-term impairments in the Tc1 mouse model of Down syndrome. *Learn. Mem.* 2008; 15:492–500. [PubMed: 18626093]
19. Rolls ET. A computational theory of episodic memory formation in the hippocampus. *Behav Brain Res.* 2010; 215:180–196. [PubMed: 20307583]
20. Henze DA, Wittner L, Buzsaki G. Single granule cells reliably discharge targets in the hippocampal CA3 network in vivo. *Nat. Neurosci.* 2002; 5:790–795. [PubMed: 12118256]
21. Hanson JE, Madison DV. Imbalanced pattern completion vs. separation in cognitive disease: network simulations of synaptic pathologies predict a personalized therapeutics strategy. *BMC Neurosci.* 2010; 11:96. [PubMed: 20704756]
22. Nicoll RA, Schmitz D. Synaptic plasticity at hippocampal mossy fiber synapses. *Nat. Rev. Neurosci.* 2005; 6:863–876. [PubMed: 16261180]
23. Bourne JN, Harris KM. Coordination of size and number of excitatory and inhibitory synapses results in a balanced structural plasticity along mature hippocampal CA1 dendrites during LTP. *Hippocampus.* 2011; 21:354–373. [PubMed: 20101601]
24. Acsady L, Kamondi A, Sik A, Freund T, Buzsaki G. GABAergic cells are the major postsynaptic targets of mossy fibers in the rat hippocampus. *J. Neurosci.* 1998; 18:3386–3403. [PubMed: 9547246]
25. Scott R, Lalic T, Kullmann DM, Capogna M, Rusakov DA. Target-cell specificity of kainate autoreceptor and Ca²⁺-store-dependent short-term plasticity at hippocampal mossy fiber synapses. *J. Neurosci.* 2008; 28:13139–13149. [PubMed: 19052205]
26. Cheng J, Ji D. Rigid firing sequences undermine spatial memory codes in a neurodegenerative mouse model. *eLife.* 2013; 2:e00647. [PubMed: 23805379]
27. Cabral HO, et al. Oscillatory dynamics and place field maps reflect hippocampal ensemble processing of sequence and place memory under NMDA receptor control. *Neuron.* 2014; 81:402–415. [PubMed: 24462101]
28. Niewoehner B, et al. Impaired spatial working memory but spared spatial reference memory following functional loss of NMDA receptors in the dentate gyrus. *Eur. J. Neurosci.* 2007; 25:837–846. [PubMed: 17313573]
29. Belichenko NP, et al. The "Down syndrome critical region" is sufficient in the mouse model to confer behavioral, neurophysiological, and synaptic phenotypes characteristic of Down syndrome. *J. Neurosci.* 2009; 29:5938–5948. [PubMed: 19420260]
30. Park J, Song WJ, Chung KC. Function and regulation of Dyrk1A: towards understanding Down syndrome. *Cell. Mol. Life Sci.* 2009; 66:3235–3240. [PubMed: 19685005]
31. Ferrer I, Gullotta F. Down's syndrome and Alzheimer's disease: dendritic spine counts in the hippocampus. *Acta Neuropathologica.* 1990; 79:680–685. [PubMed: 2141748]
32. McHugh TJ, et al. Dentate gyrus NMDA receptors mediate rapid pattern separation in the hippocampal network. *Science.* 2007; 317:94–99. [PubMed: 17556551]
33. Lanfranchi S, Carretti B, Spano G, Cornoldi C. A specific deficit in visuospatial simultaneous working memory in Down syndrome. *J. Intellect. Disabil. Res.* 2009; 53:474–483. [PubMed: 19396941]

34. Guidi S, et al. Neurogenesis impairment and increased cell death reduce total neuron number in the hippocampal region of fetuses with Down syndrome. *Brain Pathology*. 2008; 18:180–197. [PubMed: 18093248]
35. Smith GK, Kesner RP, Korenberg JR. Dentate gyrus mediates cognitive function in the Ts65Dn/DnJ mouse model of down syndrome. *Hippocampus*. 2014; 24:354–362. [PubMed: 24339224]
36. Jones MW, McHugh TJ. Updating hippocampal representations: CA2 joins the circuit. *Trends Neurosci*. 2011; 34:526–535. [PubMed: 21880379]
37. Hanson JE, Blank M, Valenzuela RA, Garner CC, Madison DV. The functional nature of synaptic circuitry is altered in area CA3 of the hippocampus in a mouse model of Down's syndrome. *J. Physiol*. 2007; 579:53–67. [PubMed: 17158177]
38. Witton J, Brown JT, Jones MW, Randall AD. Altered synaptic plasticity in the mossy fiber pathway of transgenic mice expressing mutant amyloid precursor protein. *Molecular Brain*. 2010; 3:32. [PubMed: 21040543]
39. Gardiner KJ. Molecular basis of pharmacotherapies for cognition in Down syndrome. *Trends Pharmacol. Sci*. 2010; 31:66–73. [PubMed: 19963286]
40. Fernandez F, et al. Pharmacotherapy for cognitive impairment in a mouse model of Down syndrome. *Nat. Neurosci*. 2007; 10:411–413. [PubMed: 17322876]
41. Kishnani PS, et al. Donepezil for treatment of cognitive dysfunction in children with Down syndrome aged 10-17. *Am. J. Med. Genet*. 2010; 152A:3028–3035. [PubMed: 21108390]
42. Conners FA, Rosenquist CJ, Arnett L, Moore MS, Hume LE. Improving memory span in children with Down syndrome. *J. Intellect. Disabil. Res*. 2008; 52:244–255. [PubMed: 18261023]
43. Contestabile A, Benfenati F, Gasparini L. Communication breaks-Down: from neurodevelopment defects to cognitive disabilities in Down syndrome. *Prog. Neurobiol*. 2010; 91:1–22. [PubMed: 20097253]
44. Fiala JC, Harris KM. Cylindrical diameters method for calibrating section thickness in serial electron microscopy. *J. Microscopy*. 2001; 202:468–472.
45. Nevian T, Helmchen F. Calcium indicator loading of neurons using single-cell electroporation. *Pflugers Archiv*. 2007; 454:675–688. [PubMed: 17334778]
46. Scott R, Rusakov DA. Main determinants of presynaptic Ca²⁺ dynamics at individual mossy fiber-CA3 pyramidal cell synapses. *J. Neurosci*. 2006; 26:7071–7081. [PubMed: 16807336]
47. Schmitzer-Torbert N, Jackson J, Henze D, Harris K, Redish AD. Quantitative measures of cluster quality for use in extracellular recordings. *Neuroscience*. 2005; 131:1–11. [PubMed: 15680687]

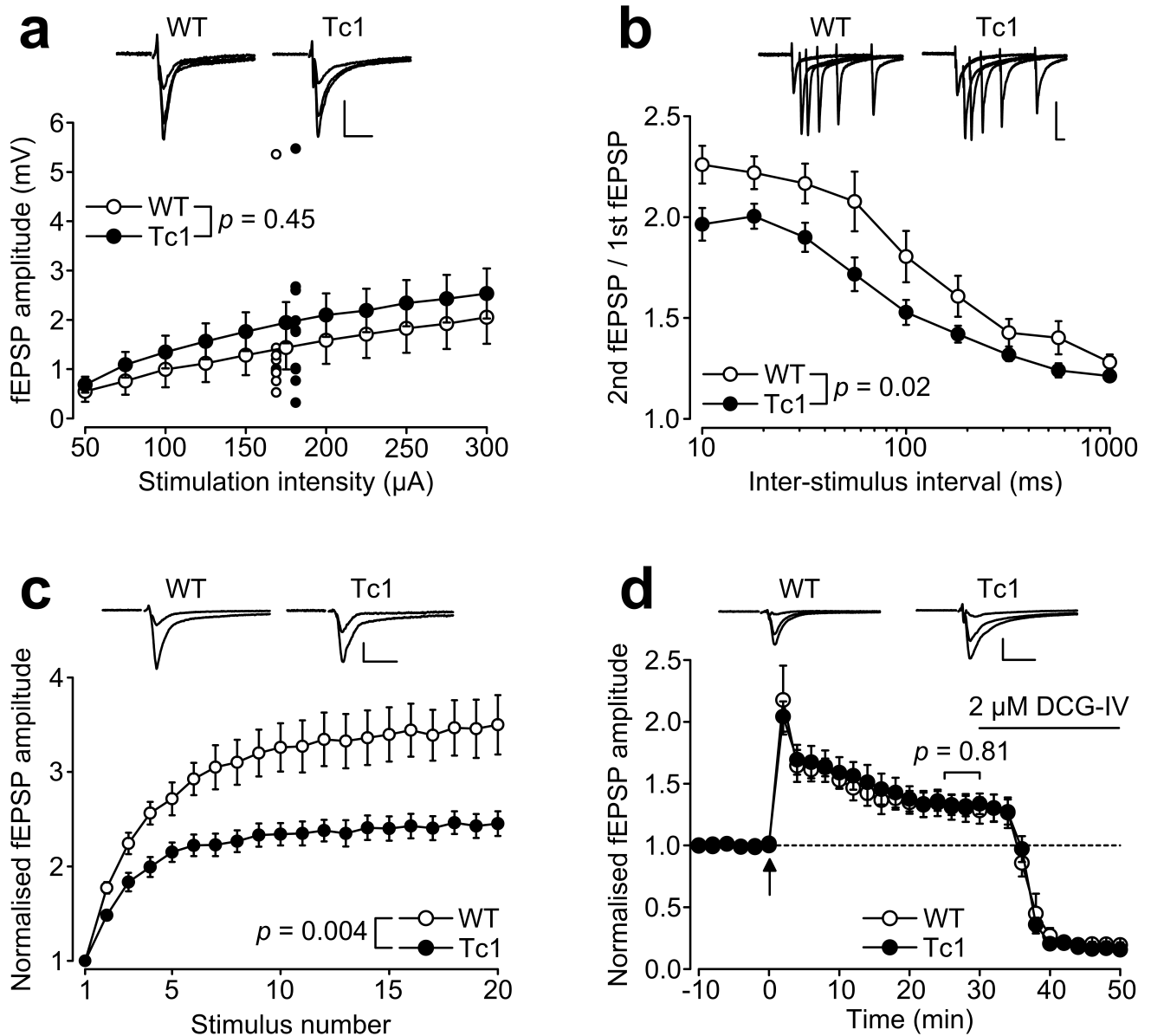


Figure 1. Altered short-term but not long-term synaptic potentiation in the mossy fiber pathway of Tc1 mice

(a) Pooled MF-CA3 stimulus-response curves in hippocampal slices from wild-type (WT, $n=10$) and Tc1 ($n=11$) mice ($p=0.45$, two-way ANOVA). Smaller circles show fEPSP amplitudes in response to $175\mu\text{A}$ stimulation for individual mice to illustrate spread of the data. Inset traces illustrate overlaid example responses to 50, 150 and $300\mu\text{A}$ stimulation for the two genotypes. Scale bar: 10ms, 0.5mV. (b) Pooled data for mossy fiber paired-pulse facilitation over inter-stimulus intervals from 10-1000ms ($p=0.02$, two-way ANOVA). Example traces illustrate responses to paired stimuli delivered over inter-stimulus intervals of 10-100ms, with a quarter log spacing. Scale bar: 10ms, 0.5mV. (c) Mossy fiber frequency facilitation during a 1Hz train of 20 pulses ($p=0.004$, two-way ANOVA). The Y-ordinate plots the amplitude of the n^{th} fEPSP of the train normalised to the amplitude of the 1^{st}

response. Example traces show overlaid recordings of the 1st and 20th traces from wild-type and Tc1 mice. Scale bar: 10ms, 0.5mV. **(d)** Pooled mossy fiber LTP data from 4 wild-type and 4 Tc1 mice ($p=0.81$, unpaired t-test). Arrow denotes timing of tetanic stimulation (1s, 100Hz repeated 3x at 10s intervals). fEPSP amplitude was recorded for 30 min following tetanisation to measure LTP. Suppression following application of 2 μ M DCGIV confirmed that fEPSPs were predominantly driven by mossy fibers. Example traces show recordings from wild-type and Tc1 mice at 0min, 30min and 50min. Scale bar: 10ms, 0.5mV. Symbols and error bars show mean \pm SEM.

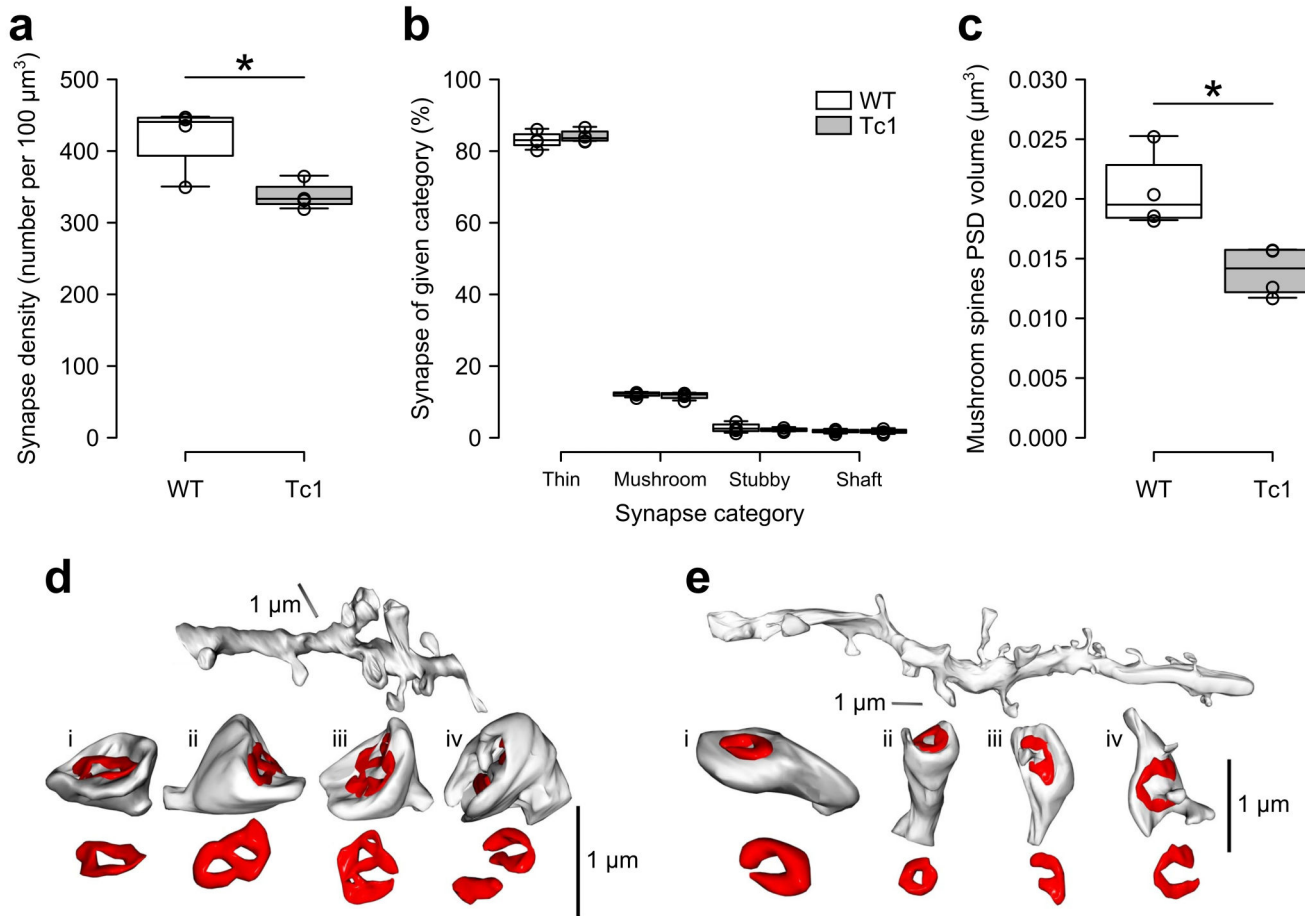


Figure 2. Reduced synapse density and post-synaptic density (PSD) volume in the middle molecular layer of dentate gyrus in Tc1 mice

(a) Overall synapse densities per $100\mu\text{m}^3$ ($p=0.02$, ANOVA), (b) distributions of four categories of spine and (c) PSD volumes ($p=0.01$, ANOVA) in wild-type (WT, $n=4$) and Tc1 mice ($n=4$). Values for individual mice (open circles) are overlaid on box-and-whisker plots. (d-e) 3-D reconstructions of dendritic segments and their mushroom spines with PSDs (red) in WT (d) and Tc1 (e) mice, exemplifying reduced PSD volumes in Tc1 animals.

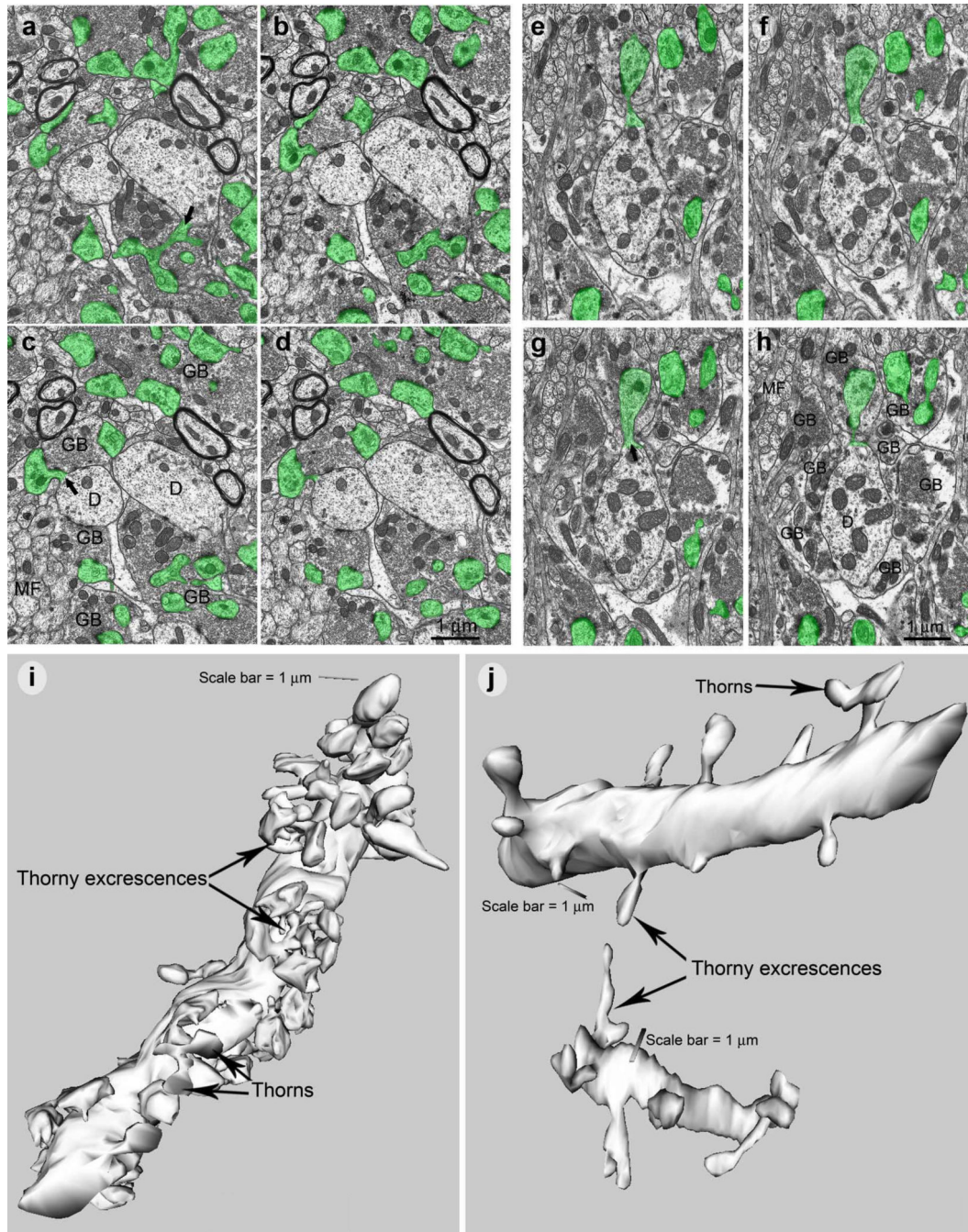


Figure 3. 3-D reconstruction of CA3 pyramidal cell dendrites reveals loss of thorny excrescences in Tc1 mice

Consecutive images of proximal portions of CA3 dendrites for both wild-type (a-d) and Tc1 mice (e-h). Thorny excrescence profiles are labelled in green, exemplifying a clear reduction of thorns in Tc1 mice. Abbreviations: **D**, dendritic shafts; **GB**, mossy fiber giant boutons or varicosities representing pre-synaptic portions of the synapses; **MF**, mossy fibers or axons originating from granule cells. 3-D reconstructed CA3 dendritic segments with thorny excrescences in (i) wild-type and (j) Tc1 mice.

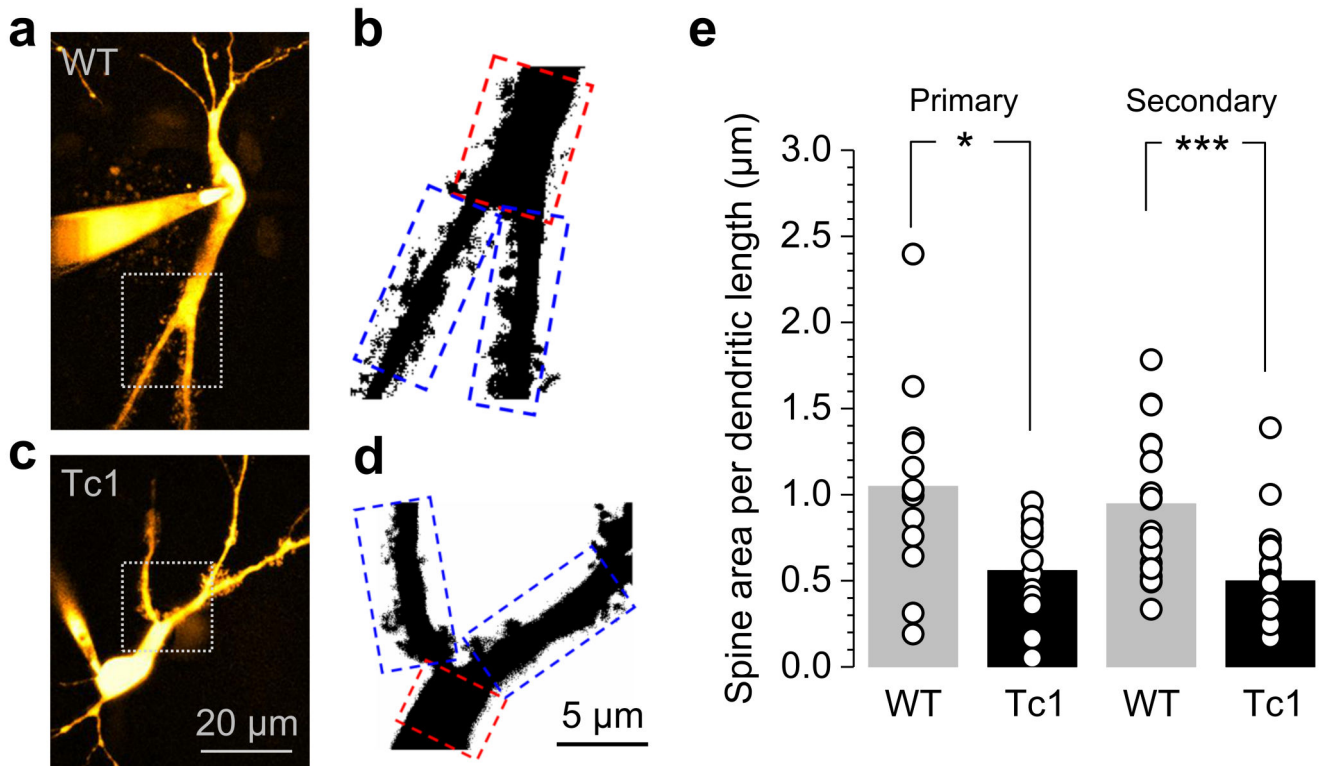


Figure 4. Adult Tc1 mice show reduced postsynaptic thorny excrescences in live CA3 pyramidal cells

(a) An example of a wild-type (WT) CA3 pyramidal cell held in whole-cell mode (50μM Alexa Fluor 594; $\lambda_x^{2P}=800\text{nm}$). (b) The proximal dendritic segment of interest (marked in (a) by rectangle), with an unsupervised threshold applied. Red and blue dashed rectangles show the primary apical dendrite and second order dendrites respectively used for assessing the extent of thorny excrescences. (c–d) Examples as in (a–b), but from a Tc1 mouse. (e) Individual (open circles) and mean (bars) area per dendritic length for thorny excrescences in primary dendrites ($n=15$ and $n=16$ cells for wild-type and Tc1 respectively; $p=0.01$, unpaired t-test) and secondary dendrites ($n=23$ and 28 ; $p=2.7e^{-4}$).

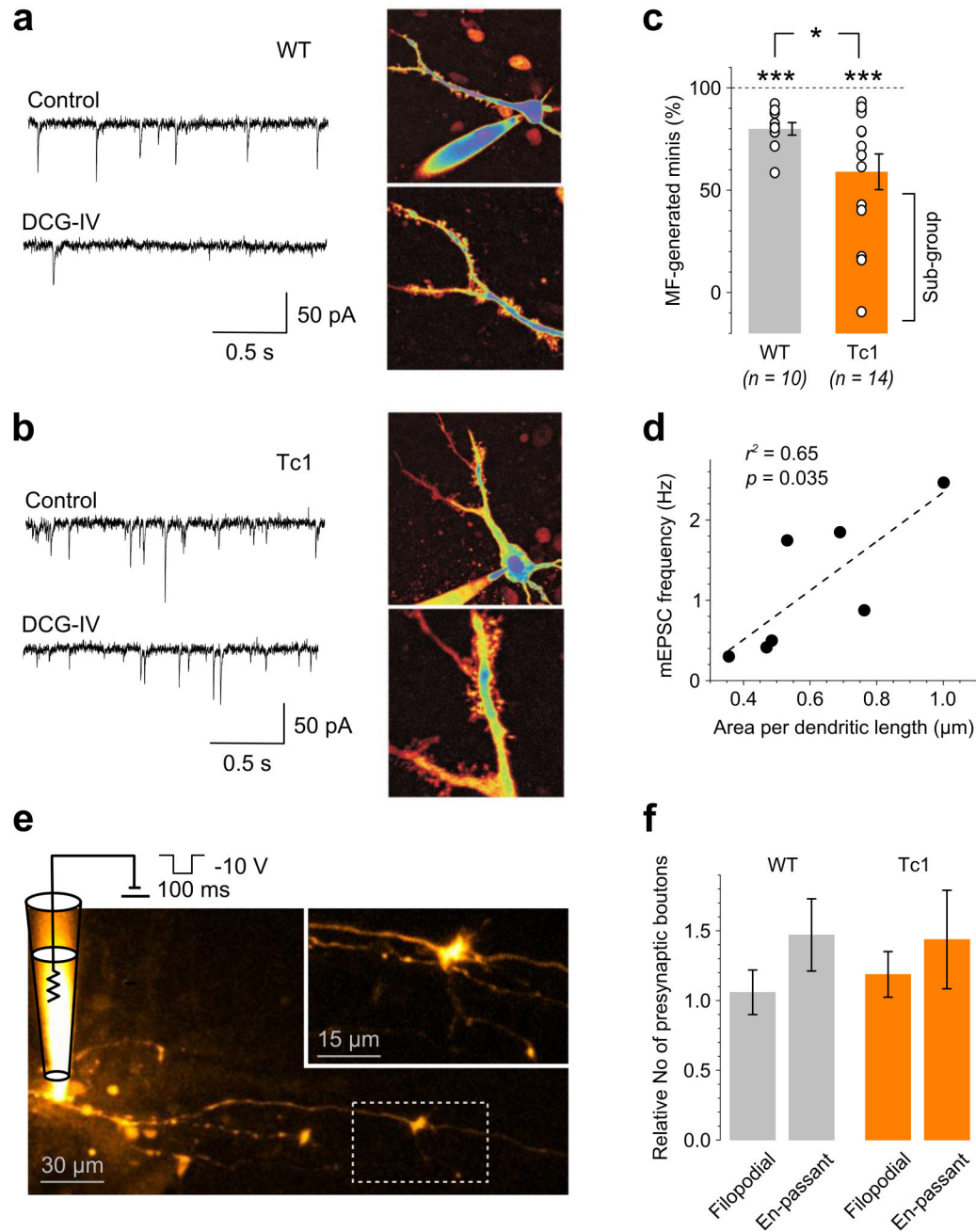


Figure 5. Reduced contribution of mossy fiber input to CA3 pyramidal cell mEPSCs in Tc1 mice (a) Left, example 2s traces from a representative wild-type CA3 pyramidal neuron illustrating mEPSCs recorded in control conditions and during application of $2\mu\text{M}$ DCG-IV; the fluorescence image (right) depicts the extent of thorny excrescences on this cell's apical dendrites. (b) Equivalent example for a Tc1 CA3 pyramidal cell exemplifying the reduced sensitivity of mEPSC frequency to DCG-IV application. (c) Group data showing average proportion (individual values in open circles, bars show mean \pm SEM) of DCG-IV-sensitive mEPSCs in wild-type (WT, $n=10$ cells from 8 mice; $p=1.0\text{e-}4$ compared to 100%, paired t-

test) and Tc1 (n=14 cells from 9 mice; $p=4.1e-4$) CA3 pyramidal cells ($p=0.04$, unequal variances test). Square bracket highlights subgroup of DCG-IV insensitive cells in Tc1 mice. **(d)** The proportion of DCG-IV-sensitive mEPSCs was positively correlated with the area of thorny excrescences on a cell-by-cell basis (linear regression $p=0.035$, Pearson's r^2 shown). **(e)** Example of electroporation labelling of MFs in CA3: a voltage pulse applied through a patch-pipette electroporates several live MFs loading them with Alexa Fluor 594; inset shows the fragment in dotted rectangle enlarged. Stars, white and yellow arrows depict 2D projection views of typical MF giant, en-passant and filopodial boutons, respectively (identified in 3D stacks and counted blind). **(f)** Average numbers of identifiable filopodial MF boutons (per one MF giant bouton) and en-passant boutons (per 25 μ m of MF length) in the two genotypes, as indicated (mean \pm SEM; n=17, 17, 16, 16 quasi-randomly sampled axonal fragments, left-to-right; WT-Tc1 group comparisons between filopodial and en-passant samples give $p = 0.583$ and $p = 0.752$, respectively, rank sum test).

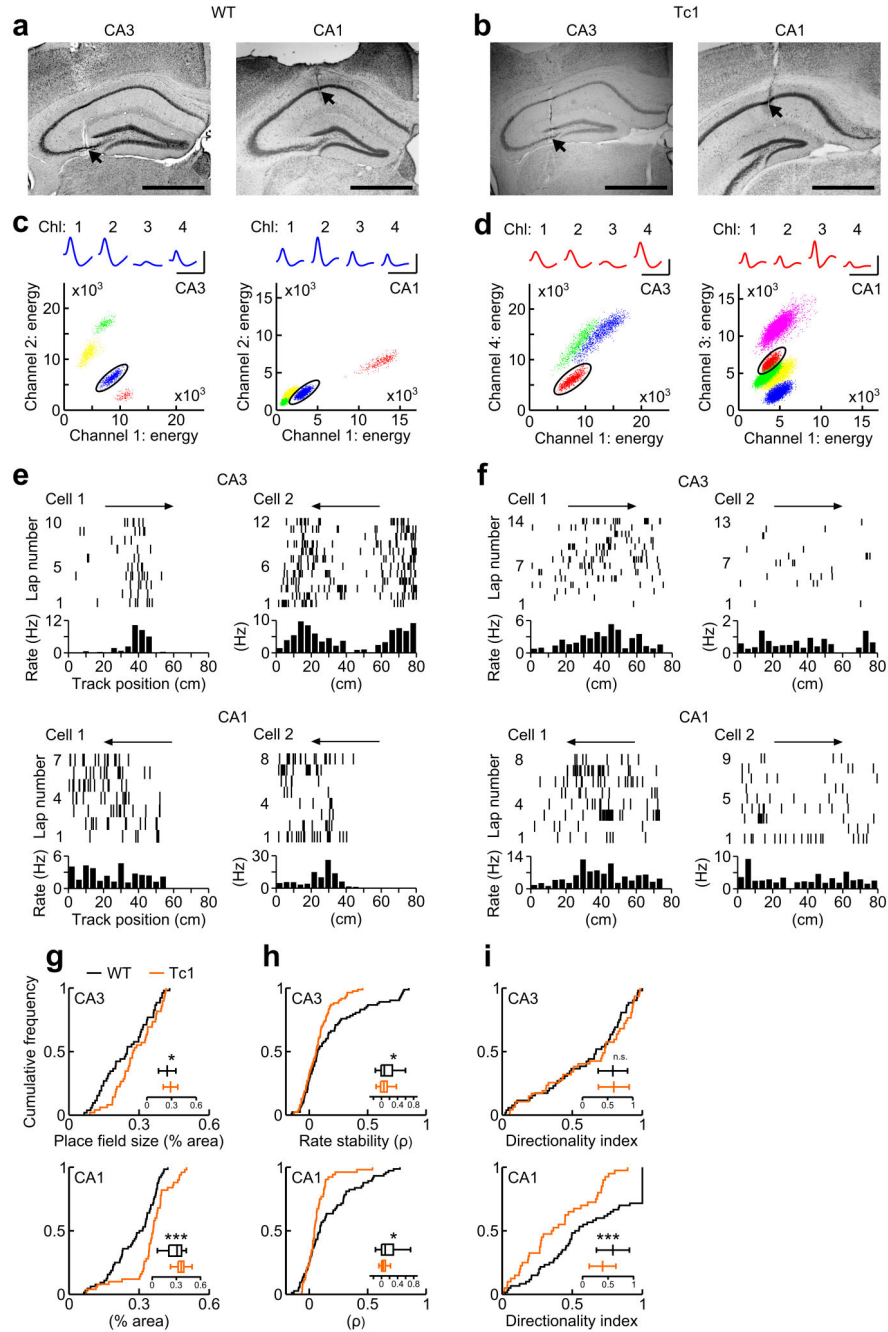


Figure 6. Impaired spatial information coding by CA3 and CA1 place cells in Tc1 mice (a–b) Photomicrographs of Nissl stained coronal brain sections illustrating tetrode tracts terminating in the CA3 and CA1 pyramidal cell layers (arrows) in (a) wild-type (WT) and (b) Tc1 mice. Scale bar: 1mm. (c–d) Scatter plots illustrating the waveform energies of extracellular action potentials recorded on two channels of representative (c) wild-type and (d) Tc1 CA3 and CA1 tetrodes. Colours highlight clusters of action potentials discharged by individual neurons. Mean action potential waveforms on each tetrode channel are illustrated for the circled clusters above their respective scatter plot. Scale bars: wild-type – 1ms,

200 μ V (CA3), 50 μ V (CA1); Tc1 – 1ms, 100 μ V (CA3), 250 μ V (CA1). **(e)** Trial-by-trial spatial firing for two representative wild-type CA3 (top) and CA1 (bottom) pyramidal cells; a single running direction is plotted for each cell, illustrated by arrows above raster plots. Track positions are plotted on the x -axis, with each tick representing the firing position of an action potential. Trial-averaged positional firing rate histograms are plotted below. **(f)** Trial-by-trial raster plots and mean positional firing rates for two representative Tc1 CA3 and CA1 pyramidal cells, showing more spatially diffuse firing and reduced inter-trial firing stability. **(g–i)** Cumulative frequency plots illustrating the distributions of **(g)** place field sizes (CA3: $p = 0.039$, unpaired t -test; CA1: $p = 3.5e^{-4}$, Rank sum test), **(h)** trial-by-trial rate stabilities (CA3: $p = 0.048$; CA1: $p = 0.042$, Rank sum test) and **(i)** directionality indices (CA3: $p = 0.757$; CA1: $p = 0.001$, unpaired t -test) for wild-type and Tc1 CA3 and CA1 pyramidal neurons. Inset box plots show the median, first and third quartiles, and 99% confidence limits; inset line plots (for normally distributed data) show the mean and standard deviation. ^{n.s.} $p > 0.05$, * $p < 0.05$, *** $p < 0.005$.

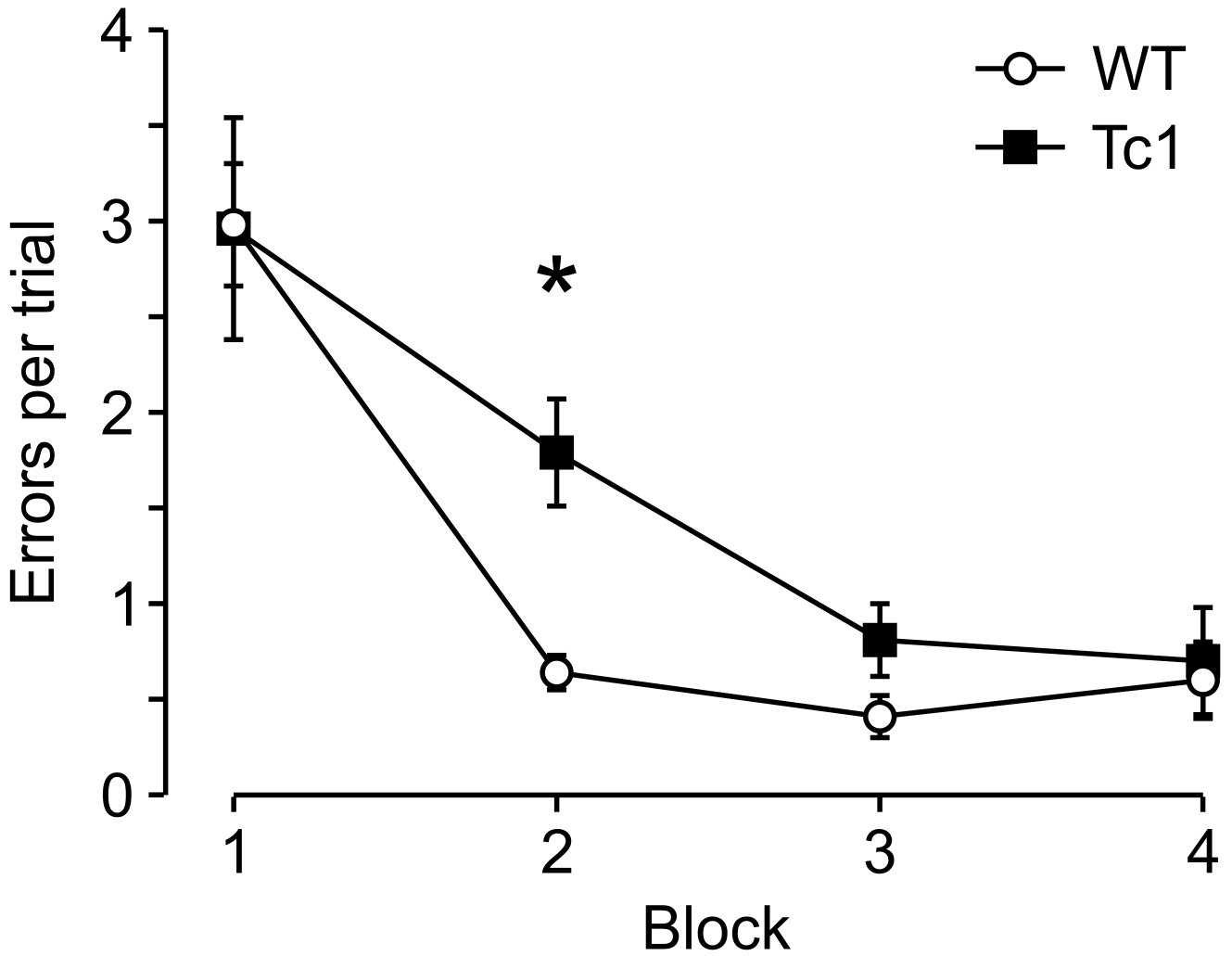


Figure 7. Tc1 mice show impaired spatial working memory on the radial arm maze
Mean ± SEM errors per trial for wild-type (WT; n=11) and Tc1 (n=9) mice on the spatial working memory, win-shift radial maze task. Blocks consist of 6 trials (1 trial per day); *p=0.004, two-way ANOVA with post-hoc test for main effect.